Formation of a Staircase Pedestal with Suppressed Edge-Localized-Modes (ELMs) in the DIII-D Tokamak

Arash Ashourvan[1], R. Nazikian[1], E. Belli[2], J. Candy[2], D. Eldon[2], B.A. Grierson[1], W. Guttenfelder[1], S.R. Haskey[1], C. Lasnier[3], G.R. McKee[4], and C.C. Petty[2]

[1] *Princeton Plasma Physics Laboratory, Princeton, New Jersey 08540, USA*

[2] *General Atomics, PO Box 85608, San Diego, CA 92186-5608, USA*

[3] *Lawrence Livermore National Laboratory, 7000 East Ave, Livermore, CA 94550, USA*

[4] *University of Wisconsin-Madison, 1500 Engineering Dr., Madison, WI 53706, USA*

The standard paradigm for the H-mode transition is the formation of an edge transport barrier when the E×B velocity shear is sufficient to suppress long wavelength instabilities [1]. Recent theoretical studies [2, 3] suggest that as we move to reactor scale with smaller $\rho^* = \rho_s/a$ (ρ_s ion sound radius, a minor radius), the E×B shear generated by the pressure gradient may be insufficient to suppress long wavelength instabilities in the pedestal, with potentially deleterious effects on H-mode confinement [2].

In a recent study it has been shown that n=3 Resonant Magnetic Perturbations (RMPs) suppress large amplitude edge-localized-modes (ELMs) in DIII-D high β_p ($\beta_p > 1.5$) plasmas leaving residual high frequency ELMs known as "grassy"-ELMs in a naturally wide pedestal regime [4]. These plasmas typically have double the edge pressure and pedestal width of ITER baseline plasmas with similar shape, toroidal field, and total stored energy (≈1 MJ) [4, 5]. The pedestal oscillates between a staircase and single step structure every 40-60 ms, correlated with oscillations in the heat and particle flux to the divertor [4].

In this work we show that for the grassy-ELM regime, periodic flattening of the density and temperature profiles occur at the onset of broadband density fluctuation at mid-pedestal. The fluctuations do not destroy the H-mode barrier, but instead create a flat spot in the middle of the barrier with the pressure gradient on either side essentially unchanged. The periodic flattening at the mid-pedestal radius results in a staircase pedestal profile and increased pedestal pressure.

Broadband fluctuations from BES measurements at the pedestal top ($\rho \approx 0.85$) and at

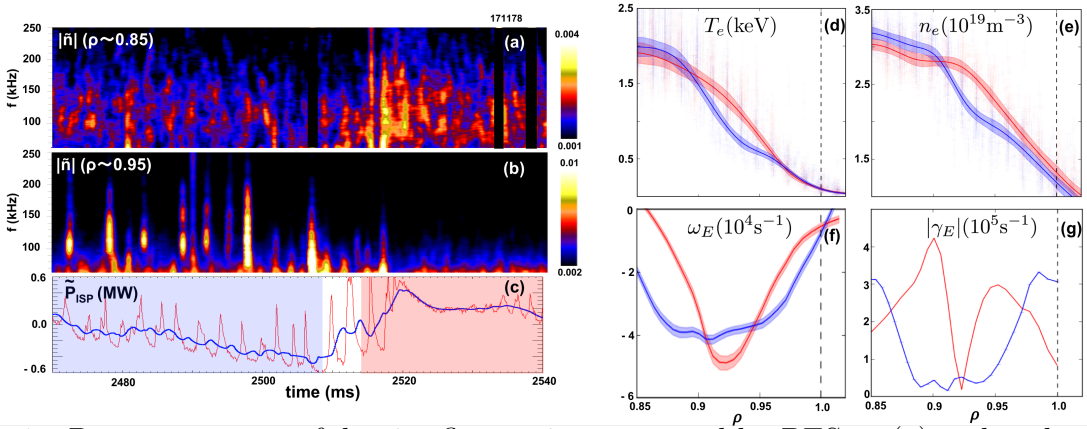

FIG. 1: Power spectrum of density fluctuation measured by BES at (a) pedestal top (b) mid-pedestal. (c) heat flux $\tilde{P}_{\mathrm{ISP}}$ at the inner strike point. Figures (d)-(g) are respectively, electron temperature electron density E×B toroidal rotation frequency (ω_E), E×B shearing rate (γ_E).

the mid-pedestal ($\rho \approx 0.95$) are shown in Figs. 1a and 1b respectively for t=2460 to 2540 ms. The modulations in the heat flux to the inner strike point (with ≈ 2 MW subtracted) is shown in Figure 1c (red) together with a 2 ms average of the heat flux (blue). Here, the high frequency peaks in the heat flux are due to grassy-ELMs. The increase in the smoothed heat flux to the inner strike point is correlated with the increase in the amplitude of turbulent fluctuation at the top of the pedestal ($\rho \approx 0.85$). The enhanced fluctuations are correlated with the periodic resonant field penetration at the pedestal top as discussed in Ref. [4]. In contrast, the bursting broadband fluctuations (f≈40-160 kHz) at the mid-pedestal ($\rho \approx 0.95$) occur during the period of decreasing heat flux to the divertor. Pedestal profiles are shown in Fig. 2(d-g). The blue profiles correspond to the period of decreasing heat flux to the divertor (blue shaded region in Fig. 2c), and the red profiles correspond to the period of increasing heat flux to the divertor (red shaded region in Fig. 2c). These profiles are obtained by ensemble averaging over 10 similar periods of these pedestal oscillation. The E×B rotation frequency ($\omega_E = E_r/RB_p$) and E×B shearing rate $\gamma_E = r/q\partial_r\omega_E$ (r, q minor radius and safety factor) are obtained from radial force balance using the CER data. During the interval of increasing heat and particle flux (red shaded region in Fig. 2c) the pedestal width contracts to $\Delta\rho \approx 0.08$ (compared to $\Delta\rho \approx 0.12$ for the staircase pedestal). The narrower pedestal has a typical Tanh shape that we call the *one-step* pedestal. During the interval of decreasing heat flux we observe a two-step structure that we call the *staircase* pedestal resulting from the strong flattening of profiles at mid-pedestal.

Local nonlinear and quasilinear gyrokinetic simulations using the CGYRO code in Fig. 2

shows a non-monotonic flux gradient relation at the mid-pedestal. From nonlinear ion-scale CGYRO simulations at $\rho = 0.95$, doubling the gradients for the staircase pedestal leads to a large increase in fluxes as shown by square open symbols in Fig. 2 consistent with a stable flux-gradient relation. The open circles in Fig. 2 show the flux versus inverse scale length for the one-step and an intermediate pedestal which is obtained by broadening and raising the height of the one-step pressure pedestal by ≈%20, and self-consistently broadening the ω_E profile. As a result, $|\gamma_E|$ of the intermediate pedestal is reduced by≈%40 compared to the experimental profile. Nonlinear ion-scale CGYRO simulations at $\rho = 0.95$ shows that even though the profile gradients have been relaxed, due to the reduced $|\gamma_E|$, fluxes in all channels dramatically increases (Q_e, Q_i and Γ_e) for the intermediate compared to one-step pedestal simulations. The negative slope demonstrates an unstable flux gradient relation. The KBM critical gradient is shown by the vertical dashed line in Fig. 2, which is within 10% of the measured gradient at mid-pedestal. Quasilinear flux calculation (dashed curve, $D = D_0(1 - \gamma_E/\gamma)$,$\Gamma = -\max[D]\nabla$n [6]) qualitatively captures the stable and unstable trends in the flux-gradient relation obtained by nonlinear simulations.

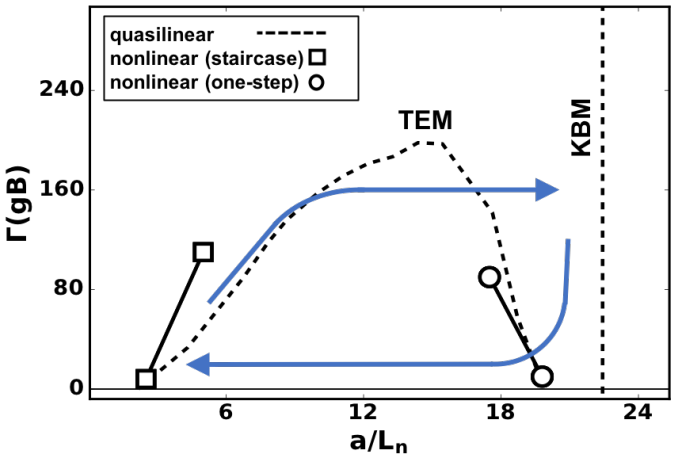

FIG. 2: Local particle flux versus a/L_n at $\rho = 0.95$. Squares and circle are the nonlinear fluxes, and dashed lines are from quasilinear calculation.

The transport bifurcation dynamics can be elucidated from the left pointing and right pointing blue arrows in Fig. 2. Starting from the staircase pedestal at $a/L_n = 2.5$ (lower left), an increase in the turbulence at the top of the pedestal increases the flux through the pedestal, driving an increase in the gradients and producing the trajectory of the upward right pointing blue arrow. This is the phase when the transport at the mid-pedestal is dominated by ITG/TEM. When the gradient increases beyond a critical threshold [7] the profile transitions to the KMB limit, owing to E×B shear suppression of ITG/TEM transport. Conversely, as the flux decreases, the gradients relax from the KBM limit to the unstable flux-gradient region. This leads to a bifurcation of the profile from the one-step to the staircase pedestal as indicated by

the blue left pointing arrow. This bifurcation corresponds to enhanced TEM transport at mid-pedestal as the E×B shear relaxes. The cycle repeats so long as there is a significant modulation in the thermal and particle transport through the pedestal, which is correlated with the modulation of the turbulence at the top of pedestal (Fig. 1a) and flux to the divertor (Fig. 1c).

As noted, the E×B shearing rate decreases rapidly with increasing pedestal width, creating the conditions where pedestal transport bifurcations can occur. As $\gamma_E/\gamma \sim \rho^*$ (γ is the dominant mode growth rate) [8], we anticipate that suppression of TEM/ITG modes will not be as effective in ITER as in current devices, leading to the possible formation of a staircase pedestal as seen in DIII-D. The consequences of enhanced ITG/TEM in the ITER pedestal are not necessarily deleterious as the pedestal pressure increases in DIII-D in the staircase phase. Therefore the consequence of staircase pedestal formation in ITER or future reactors could be beneficial for confinement.

This material is based upon work supported by the U.S. Department of Energy, Office of Science, Office of Fusion Energy Sciences, using the DIII-D National Fusion Facility, a DOE Office of Science user facility, under Awards DE-FC02-04ER54698 and DE-AC02-09CH11466

[1] K. H. Burrell, Plasma Phys. Controlled Fusion **36**, A291 (1994).
[2] M. Kotschenreuther, D. Hatch, S. Mahajan, P. Valanju, L. Zheng, and X. Liu, Nucl. Fusion **57**, 064001 (2017).
[3] D. Hatch, D.Told, F. Jenko, H. Doerk, M. Dunne, E. Wolfrum, E. Viezzer, The ASDEX Upgrade Team3, and M. Pueschel, Nucl. Fusion **55**, 063028 (2015).
[4] R. Nazikian, C. Petty, A. Bortolon, X. Chen, D. Eldon, T. Evans, B. Grierson, N. Ferarro, S. Haskey, M. Knolker, C. Lasnier, N. Logan, R. Moyer, D. Orlov, T. Osborne, C. Paz-Soldan, F. Turco, H. Wang, and D. Weisberg, Nucl. Fusion **58**, 106010 (31pp) (2018).
[5] G. L. Jackson, P. A. Politzer, D. A. Humphreys, T. A. Casper, A. W. Hyatt, J. A. Leuer, J. Lohr, T. C. Luce, M. A. V. Zeeland, and J. H. Yu, Phys. Plasmas **17**, 056116 (2005).
[6] F. Jenko, T. Dannert, and C. Angioni, Plasma Phys. Controlled Fusion **47**, B195 (2005).
[7] V. Lebedev and P. Diamond, Phys. Plasmas **4**, 1087 (1997).
[8] R. E. Waltz, G. D. Kerbel, J. Milovich, and G. W. Hammett, Phys. Plasmas **1**, 2229 (1994).